Subpicosecond Ultracold Electron Source

T. C. H. de Raadt[©],[*] J. G. H. Franssen[©], and O. J. Luiten

Department of Applied Physics, Eindhoven University of Technology, P.O. Box 513, 5600 MB Eindhoven, Netherlands

We present the first observation of subpicosecond electron bunches from an ultracold electron source. This source is based on near-threshold, two-step, femtosecond photoionization of laser-cooled rubidium gas in a grating magneto-optical trap. Bunch lengths as short as 735 ± 7 fs (rms) have been measured in the self-compression point of the source by means of ponderomotive scattering of the electrons by a 25 fs, 800 nm laser pulse. The observed temporal structure of the electron bunch depends on the central wavelength of the ionization laser pulse, in agreement with detailed simulations of the atomic photoionization process. This shows that the bunch length limit imposed by the atomic photoionization process has been reached.

Ultrafast, high brightness electron source development is essential for challenging applications such as ultrafast electron diffraction (UED), ultrafast electron microscopy (UEM) and x-ray free electron lasers (XFELs), which are revolutionizing science by unveiling the structural dynamics of matter at atomic length and timescales [1–3]. Conventional copper photocathodes, the workhorses of ultrafast electron and x-ray science, have reached their fundamental limits [4], and further increase of the source brightness is sought in lowering its electron temperature T or mean transverse energy (MTE) which is equal to $k_b T$, with k_b the Boltzmann constant [5,6]. The most extreme example of this approach is the so-called ultracold electron source (UCES) [7–11], which is based on near-threshold photoionization of the coldest substances known: laser-cooled and trapped atomic gases. The UCES is characterized by record-low electron source temperatures of ∼20 K (MTE of ∼2 meV), giving rise to normalized emittances as low as ∼1 nm rad for a source size of a few tens of micron, as measured in Refs. [11,12]. Its unique features raise exciting prospects such as single-shot protein crystallography [13–16] and tabletop quantum free electron lasers [17]. For such applications the temporal properties of the electron bunches are of the utmost importance. In previous work 25 ps bunch lengths were achieved in the beamline 68 cm from the source, measured using a 3 GHz deflection cavity [18]. Here, we will demonstrate bunch lengths as short as 735 fs, measured using pondermotive scattering of the electrons [19–26] by a 25 fs, 800 nm laser

pulse, inside a longitudinal waist of the electron beam at 18 mm from the ionization volume. This so-called self-compression point is a unique feature of the UCES [7]. The observed temporal structures of the electron bunches agree with detailed simulations of the atomic photoionization process [12,18,27,28], showing that a fundamental bunch length limit imposed by the atomic photoionization process has been achieved. As a result, the longitudinal emittance is limited by the photoionization process rather than the electron temperature. Therefore, the initial 6D phase space distribution is now fully understood, both transversally and longitudinally, allowing ultimate control of the UCES bunches in all three dimensions.

The latest generation UCES developed at the Eindhoven University of Technology [11] is schematically illustrated in Fig. 1. It utilizes a novel grating technique [29,30] to achieve a four beam rubidium-85 magneto-optical trap
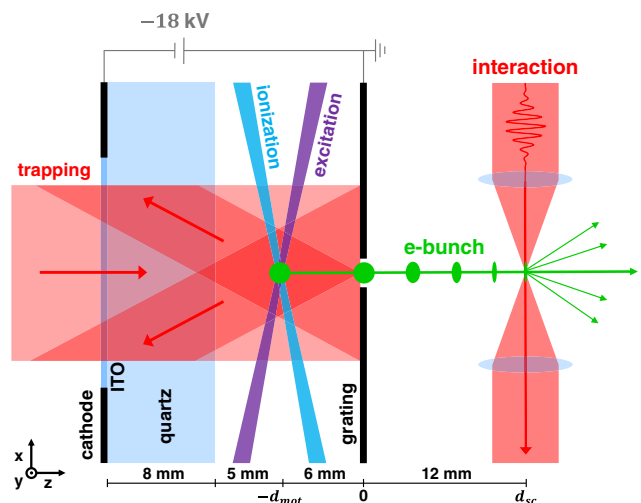

FIG. 1. Schematic representation of the UCES setup.

(MOT) using only a single 780 nm continuous trapping laser beam. Within the overlap volume of the four laser beams (red), the radiation pressure balances out in all directions such that a high density $\sim 10^{16}$ m^{-3} [11] cloud of cold atoms can be formed. A two-step ionization scheme excites the atoms from the $5S^{1/2}$ ground state to the $5P^{3/2}$ intermediate state with a microsecond 780 nm laser (purple beam), and subsequently ionizes the atoms from the $5P^{3/2}$ state using a tunable femtosecond 475–495 nm laser (blue beam). Intricate 3D shaping of the initial electron distribution is enabled by the fact that ionization occurs only where the excitation and ionization laser beams overlap (green circle at $z = -d_{\text{MOT}}$ in Fig. 1), offering exquisite control over the pulsed electron beam [14].

The created electrons are immediately accelerated by a 18 kV dc potential difference between the transparent ITO-coated quartz cathode, where the trapping laser passes through, and the grounded grating surface, providing an acceleration field in the z direction of $F_{\text{acc}} = 1.2$ MV/m. The electrons pass through a 500 μm diameter hole in the center of the grating, creating electron bunches with energies up to $U_e = 10.2 \pm 0.4$ keV [11]. Repetition rates up to 1 kHz are achieved, limited by the femtosecond laser system and the MOT loading rate. The longitudinal extent of the ionization volume causes the back of the electron bunch to be accelerated over a longer distance than the front. This results in a self-compression point [7,11,18] situated at $z = d_{\text{sc}} = 2d_{\text{mot}}\sqrt{1 - (\sigma_z/d_{\text{MOT}})^2}$ in which $\sigma_z = 64$ μm is the rms length of the ionization volume and $d_{\text{MOT}} = 6$ mm the distance between the center of the trapped gas cloud and the grating surface, resulting in $d_{\text{sc}} \approx 12$ mm [31].

The bunch length in the self-compression point is determined by five contributions: the geometrical imperfection of the self-compression point (~ 7 fs), the ionization laser pulse length (~ 80 fs), the electron temperature (~ 92 fs), space charge broadening, and the photoionization time (~ 1 ps). Space charge forces start to play a role at a bunch charge of about 5×10^4 electrons, typically ten times more than was used in this work and can therefore be neglected. The estimations for the other contributions are discussed in more detail in Supplemental Material [32]. The time it takes the electrons to escape the Rb-85 atomic potential, the photoionization time, turns out to be the dominant timescale. Ponderomotive scattering of the electrons offers a high temporal resolution (~ 50 fs) and small interaction region (~ 10 μm) and is therefore the method of choice to study the temporal distribution of the bunches in the self-compression point. The ponderomotive force is given by $\vec{F}_p = -(e^2\lambda^2/8\pi^2 m_e \varepsilon_0 c^3)\nabla I_p$, where e is the electron charge, λ the laser wavelength, m_e the electron mass, ε_0 the vacuum permittivity, c the speed of light, and I_p the laser intensity. Using 1.1 mJ, 25 fs, 800 nm laser pulses, the interaction laser pulses for short, which are

focused onto the electron bunch at the self-compression point inside the vacuum chamber to a waist of 5.9 μm (see Fig. 1), a peak intensity of about $I_p = 1.1 \times 10^{16}$ W/cm^2 is achieved. The electrons scattered in the transverse direction by this interaction laser pulse are detected at the end of the beamline, 1.6 m from the MOT, using a Cheetah Timepix3 direct electron camera [46,47].

Since the temporal and spatial overlap window for ponderomotive scattering is very small, we employ a plasma-based method with the help of an aperture for first alignment (Supplemental Material [32]). The interaction laser and ionization laser originate from the same femtosecond laser system and are therefore intrinsically synchronized. The delay between the ionization laser pulses, and thus the electron bunches, and the interaction laser pulses can be varied using a linear delay stage.

Once spatial and temporal overlap is achieved within 40 ps and 100 μm, the aperture is removed for ponderomotive scattering measurements. In Figs. 2(a)–2(c) the measured bunch charge distributions are presented as a function of the time delay between the interaction laser pulse and the electron bunch arriving in the self-compression point, for central ionization laser wavelengths of 474.4, 488.7, and 498.1 nm, respectively. The central wavelength is defined as the weighted average of the spectral distribution (see Supplemental Material [32]). In the insets of Fig. 2(a) detector images are shown recorded at a delay of 0.6 ps, without interaction laser [Fig. 2(d)] and with interaction laser [Fig. 2(e)], clearly showing the ponderomotive scattering of the electrons. The number N_e of scattered electrons per bunch for a certain delay is obtained by summing the counts inside the red outlined areas in Figs. 2(d) and 2(e). The noise is reduced by removing all events outside a 150 ns window around the main electron peak, leveraging the time resolution of the Cheetah. By varying the delay between the interaction laser pulse and the electron bunch, the longitudinal charge distribution is obtained. At each time delay, three measurements are recorded: a baseline signal in which the interaction laser is blocked (black), the number of electrons scattered with the polarization of the ionization laser parallel to accelerator field (red), and with perpendicular polarization (blue), as shown in Figs. 2(a)–2(c). Taking all three measurements before continuing to the next delay minimizes the effect of drift.

For both polarizations the measured temporal bunch distribution of Fig. 2(a) is fitted by a Gaussian distribution, resulting in an rms electron bunch length of $\sigma_t = 735 \pm 7$ fs. Note that for $F_{\text{acc}} = 1.2$ MV/m, the central ionization laser wavelength of 474.4 nm lies well below the stark-shifted ionization threshold of 495.0 nm.

In the measurements shown in Figs. 2(b) and 2(c) the wavelengths used, respectively 488.7 and 498.1 nm, are much closer to the ionization threshold. Note that only the part of the spectral bandwidth which lies below 495.0 nm of
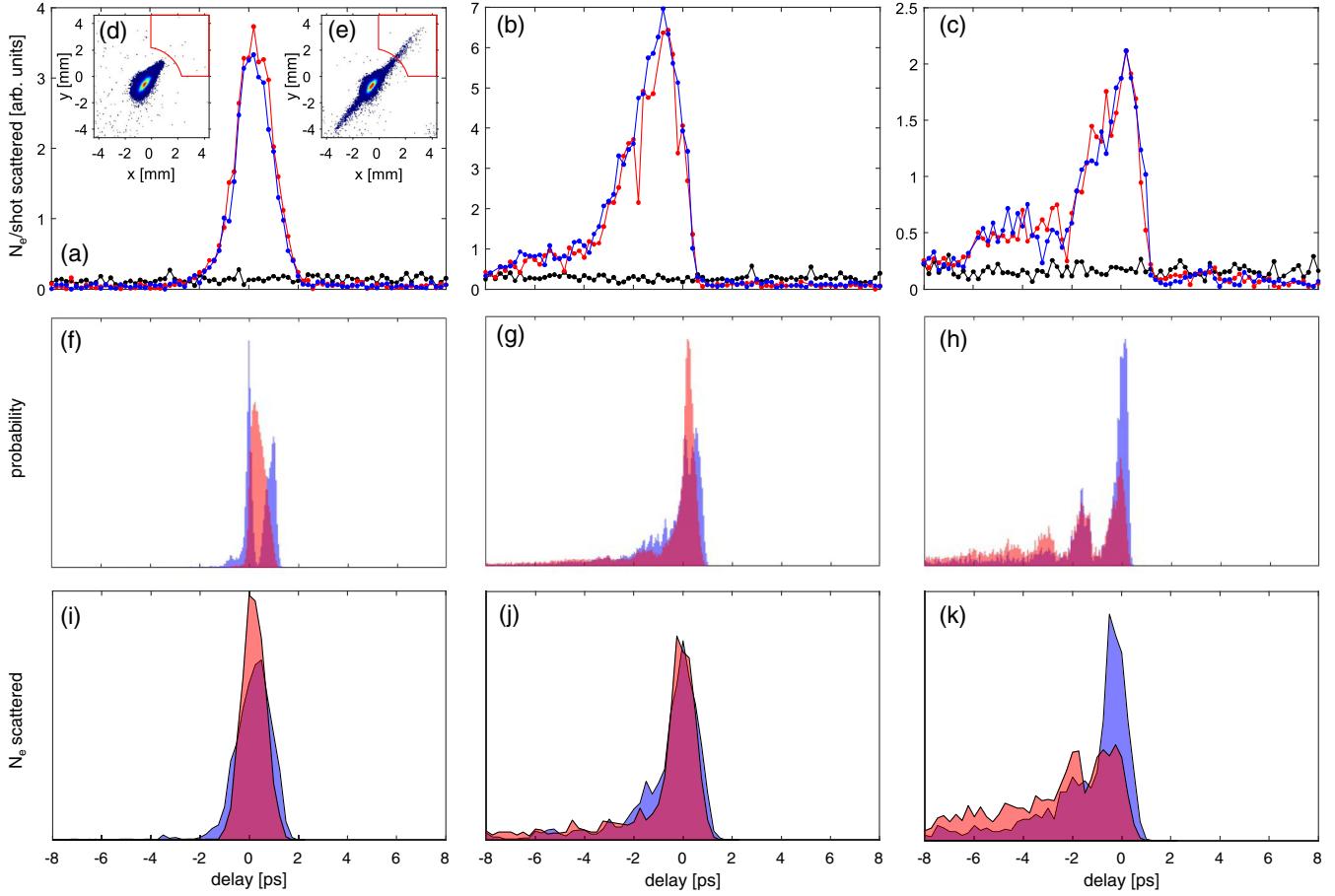
FIG. 2. (a)–(e) The measured number N_e of electrons scattered per bunch as function of the delay between the interaction laser pulse and the electron bunch in the self-compression point, with the ionization laser polarization parallel (red) and perpendicular (blue) to the accelerating field, and with central ionization wavelengths of (a) 474.4 nm, (b) 488.7 nm, and (c) 498.1 nm. Insets (d) and (e) show detector images recorded at a delay of 0.6 ps without and with interaction laser, respectively. N_e is obtained by summing the counts inside the red outlined areas in the insets (d) and (e). (f)–(h) GPT simulations of the time profiles of the atomic photoionization process of stark shifted Rb atoms in an electric field of 1.2 MV/m. In the simulations the measured laser spectra are used. (i)–(k) GPT simulations of the measured temporal distributions of the bunches in the self-compression point based on the time profiles of (f)–(h) and a realistic beamline model.

the measurement of Fig. 2(c) leads to photoionization. In Figs. 2(b) and 2(c) deviations from a Gaussian temporal bunch profile start to appear. The right flank of the temporal profile represents the fast electrons that arrive at the self-compression point first. This flank is largely unchanged compared to Fig. 2(a). The left flank, however, is washed out considerably as the ionization laser approaches the ionization threshold. This would agree with the theoretical models [18,27,28] which predict that part of the electrons created with very low excess energy (in between the zero-field and stark-shifted ionization threshold) can orbit many times around the rubidium core before they escape. This would result in a train of delayed electrons as is observed very clearly in the broadening of the left flank in Fig. 2(c).

To explain the experimental results in more detail, classical charged particle tracking simulations have been performed using the GPT code of electrons escaping the rubidium potential [48]. Figure 3 shows simulations of five

(classical) electron trajectories with different initial angles, at ionization wavelengths of 474.4 nm (red, purple, and blue trajectories), representative of the measurement of Fig. 2(a), and 492.0 nm (white trajectory), representative of Fig. 2(c). After leaving the rubidium potential, the electrons are accelerated by a constant electric field $F_{\mathrm{acc}} =$ 1.2 MV/m in the z direction. The relative arrival time at a plane 1 mm from the atomic center is indicated on each trajectory in Fig. 3. The experimental observable is the arrival time distribution, which is defined as the distribution of the time it takes for an electron to exit the atomic core at $(x, z) = (0, 0)$ and reach the plane at $z = 1$ mm. In this Letter, the width of this distribution is referred to as the photoionization time.

To simulate the measured temporal bunch distributions shown in Figs. 2(a)–2(c), 5×10^4 electron trajectories have been calculated, similar to those plotted in Fig. 3, using initial angles and excess energies derived from the
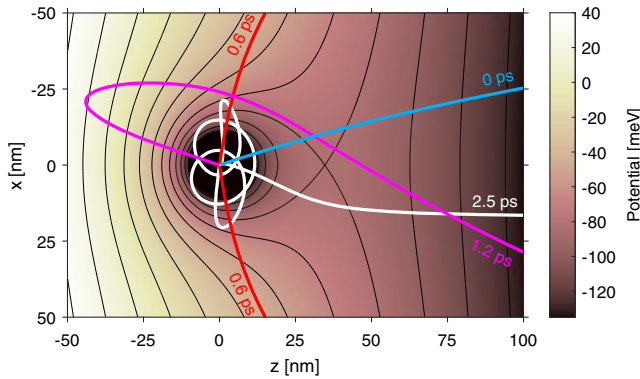
FIG. 3. GPT simulations of trajectories of electrons escaping a singly ionized rubidium atom at $(x, y) = (0, 0)$. Indicated are the (color-coded) potential energy and equipotential lines (thin black curves) due to the ionic Coulomb field in an external uniform electric field of 1.2 MV/m. Five simulated trajectories are shown (thick colored curves), corresponding to five different initial angles and ionization wavelengths of 474.4 nm (red, purple, and blue trajectories) and 492.0 nm (white trajectory). The relative arrival times at $z = 1$ mm are indicated. Note that $z = 0$ in this figure corresponds to $z = -d_{MOT}$ in Fig. 2.

ionization laser polarization directions and wavelengths. This results in a distribution of arrival times, which are plotted in Figs. 2(f)–2(h). In previous work all electrons in a simulation of the temporal distribution were initiated with the same excess energy [18,27,28], neglecting the finite laser bandwidth. In Figs. 2(f)–2(h), the measured laser spectra (Supplemental Material [32]) are used as a probability distribution for the excess energy of the electrons, giving results that more closely represent the results of Figs. 2(a)–2(c). The electric field used in the simulations is about 5 times stronger than in previous work [18,27,28], resulting in electron pulses that are about 5 times shorter. The temporal distributions of the electron bunches for the two orthogonal polarizations and the three measured wavelength profiles are shown in Figs. 2(f)–2(h).

At high excess energies [Fig. 2(f)] the electrons can escape the rubidium potential in all directions. This results in a single peak for a polarization perpendicular to the electric field [Fig. 2(f) red, Fig. 3 red]. For parallel polarization [Fig. 2(f) blue] half of the electrons directly escape the Rb potential in a positive z direction (Fig. 3, blue trajectory) while the other half is launched uphill on the electrostatic potential, turns around and then escapes the potential (Fig. 3, purple trajectory) causing two peaks [18,28,49]. At low excess energies [Fig. 2(h)] the electrons can only escape the Rb potential over the saddle point created by the stark shift. Therefore, electrons can be trapped orbiting in the potential well until they scatter on the core and have another chance to escape (Fig. 3, white curve). This creates pulse trains as shown in Fig. 2(h). The parallel polarization will have an initial high peak from half of the electrons that are ionized in the direction of the saddle point. The broad spectrum of the

femtosecond laser will broaden these pulse trains into a tail as is seen in Fig. 2(g).

Note that the GPT simulations [Fig. 2(f)], theoretical classical predictions [18,28], and experimental results on Cs [50] and Rb [49] would suggest a different temporal profile for the two orthogonal polarizations of the ionization laser. However, the measurements of Fig. 2(a) show no significant difference between the two orthogonal polarizations. Moreover, the temporal profile of Fig. 2(a) seems slightly broader than the GPT simulation of Fig. 2(f).

A possible explanation is an instrumental broadening effect. To investigate this GPT simulations have been done of bunch propagation in the beamline. These simulations were based on the simulated time profiles of the photoionization process shown in Figs. 2(f)–2(h), the measured rms sizes $\sigma_x = 126$, $\sigma_y = 75$, and $\sigma_z = 64$ μm of the ionization volume, an initial electron temperature of $T = 25$ K, as measured in [11], realistic electromagnetic field maps of the beamline elements, and the ponderomotive scattering of electrons by a realistic laser field. The resulting temporal distributions of the bunches are obtained by counting the number of scattered electrons N_e and are shown in Figs. 2(i)–2(k).

The pulse train structure in Fig. 2(h) seems to have washed out in Fig. 2(k), resulting in a trailing tail on the left flank that agrees with the measurement results shown in Fig. 2(c). Moreover, the difference between parallel and perpendicular polarization has also largely disappeared, also in agreement with experimental observations. This broadening effect can be attributed to the fact that the interaction laser comes in at an angle $\theta = \tan^{-1}(v_z/c)$ in the comoving frame of the electron bunch. A simple model predicts an increase of the bunch length of 420 fs for the parameters in this experiment. This is confirmed by GPT simulations of the ponderomotively measured bunch (see Supplemental Material [32]). In future experiments this instrumental broadening could be reduced by tilting the interaction laser beam to compensate for the fact that $\theta \neq \pi/2$. However, some discrepancies between Figs. 2(a)–2(c) and Figs. 2(i)–2(k) remain. In Figs. 2(i)–2(k) the dependence on polarization is still observable and the temporal structure is slightly narrower than in the experiments. These discrepancies may be attributed to an incomplete description of the beamline, and the classical description of the photoionization process. A fully quantum mechanical model for ionization of stark-shifted rubidium atoms would therefore be desirable.

We have gained valuable insights into the photoionization process lying at the heart of the UCES, which have important implications for its use as a high brightness electron source.

First, a simplified analytical model (see Supplemental Material [32]) shows that the photoionization time depends on a combination of the acceleration field strength, the ionization wavelength, and the ionization laser polarization.

The most efficient way to decrease the photoionization time further is to increase the acceleration field. However, the laser cooling process becomes increasingly difficult at higher acceleration fields [11].

Second, the self-compression point studied in this work constitutes a longitudinal waist as the position and momentum are uncorrelated there. This makes it the ideal place to study the longitudinal beam properties of the UCES. The normalized longitudinal emittance $\hat{\varepsilon}_z$, which is conserved throughout the beamline, is given in a waist by the product of the measured bunch length σ_t and the energy spread σ_U: $\hat{\varepsilon}_z = (\sigma_t \sigma_U / m_e c)$. Using $\sigma_U = eF_{\text{acc}} \sigma_z$ and $\sigma_t = 735$ fs we find $\hat{\varepsilon}_z = 33$ nm rad. Note that since σ_t is limited by the atomic photoionization process, the $\hat{\varepsilon}_z$ is not limited by the electron temperature T in contrast to the transverse emittance $\hat{\varepsilon}_x = \sigma_x \sqrt{(k_b T / m_e c^2)}$. The longitudinal emittance provides a lower limit of the product of σ_U and σ_t at the sample. By using, e.g., an rf compression cavity [20,21,51], the waist of the self-compression point can be longitudinally imaged at the sample. This allows the shortest possible pulses for a given energy spread, or vice versa, for applications in UEM or UED.

In conclusion, we have shown for the first time that subpicosecond ultracold electron bunches can be produced by femtosecond photoionization of a laser-cooled and trapped rubidium gas. Bunch lengths as short as 735 fs have been measured by ponderomotive scattering of electrons on 25-fs laser pulses. The high temporal resolution allowed determination of the detailed temporal structure of the bunches, clearly showing that the bunch length limit imposed by the atomic photoionization process was reached. As a result, the longitudinal emittance of the UCES is independent of the initial electron temperature and is given by the product of the atomic photoionization time and the energy spread associated with the length of the ionization volume. Since the photoionization time is ∼1 ps, the ionization laser pulse length, now ∼80 fs, can be increased by an order of magnitude without compromising the longitudinal emittance. This allows reducing the ionization laser bandwidth with an order of magnitude and thus enabling even lower electron temperatures.

---

*t.c.h.d.raadt@tue.nl

[1] G. Sciaini and R. J. D. Miller, Femtosecond electron diffraction: Heralding the era of atomically resolved dynamics, Rep. Prog. Phys. **74**, 096101 (2011).

[2] A. Adhikari, J. K. Eliason, J. Sun, R. Bose, D. J. Flannigan, and O. F. Mohammed, Four-dimensional ultrafast electron microscopy: Insights into an emerging technique, ACS Appl. Mater. Interfaces **9**, 3 (2017).

[3] N. Huang, H. Deng, B. Liu, D. Wang, and Z. Zhao, Features and futures of x-ray free-electron lasers, Innovation **2**, 100097 (2021).

[4] P. L. E. M. Pasmans, D. C. van Vugt, J. P. van Lieshout, G. J. H. Brussaard, and O. J. Luiten, Extreme regimes of femtosecond photoemission from a copper cathode in a dc electron gun, Phys. Rev. Accel. Beams **19**, 103403 (2016).

[5] L. Cultrera, S. Karkare, H. Lee, X. Liu, I. Bazarov, and B. Dunham, Cold electron beams from cryocooled, alkali antimonide photocathodes, Phys. Rev. ST Accel. Beams **18**, 113401 (2015).

[6] S. Karkare, G. Adhikari, W. A. Schroeder, J. K. Nangoi, T. Arias, J. Maxson, and H. Padmore, Ultracold Electrons via Near-Threshold Photoemission from Single-Crystal Cu (100), Phys. Rev. Lett. **125**, 054801 (2020).

[7] B. J. Claessens, S. B. van der Geer, G. Taban, E. J. D. Vredenbregt, and O. J. Luiten, Ultracold Electron Source, Phys. Rev. Lett. **95**, 164801 (2005).

[8] O. J. Luiten, B. J. Claessens, S. B. van der Geer, M. P. Reijnders, G. Taban, and E. J. D. Vredenbregt, Ultracold electron sources, Int. J. Mod. Phys. A **22**, 3882 (2007).

[9] G. Taban, M. P. Reijnders, B. Fleskens, S. B. v. d. Geer, O. J. Luiten, and E. J. D. Vredenbregt, Ultracold electron source for single-shot diffraction studies, Europhys. Lett. **91**, 46004 (2010).

[10] W. J. Engelen, E. P. Smakman, D. J. Bakker, O. J. Luiten, and E. J. D. Vredenbregt, Effective temperature of an ultracold electron source based on near-threshold photoionization, Ultramicroscopy **136**, 73 (2014).

[11] J. G. H. Franssen, T. C. H. de Raadt, M. A. W. van Ninhuijs, and O. J. Luiten, Compact ultracold electron source based on a grating magneto-optical trap, Phys. Rev. Accel. Beams **22**, 023401 (2019).

[12] W. J. Engelen, M. A. van der Heijden, D. J. Bakker, E. J. D. Vredenbregt, and O. J. Luiten, High-coherence electron bunches produced by femtosecond photoionization, Nat. Commun. **4**, 1693 (2013).

[13] S. B. van der Geer, M. J. de Loos, E. J. Vredenbregt, and O. J. Luiten, Ultracold electron source for single-shot, ultrafast electron diffraction, Microsc. Microanal. **15**, 282 (2009).

[14] A. J. McCulloch, D. V. Sheludko, S. D. Saliba, S. C. Bell, M. Junker, K. A. Nugent, and R. E. Scholten, Arbitrarily shaped high-coherence electron bunches from cold atoms, Nat. Phys. **7**, 785 (2011).

[15] A. J. McCulloch, D. V. Sheludko, M. Junker, and R. E. Scholten, High-coherence picosecond electron bunches from cold atoms, Nat. Commun. **4**, 1692 (2013).

[16] D. J. Thompson, D. Murphy, R. W. Speirs, R. M. W. van Bijnen, A. J. McCulloch, R. E. Scholten, and B. M. Sparkes, Suppression of Emittance Growth Using a Shaped Cold Atom Electron and Ion Source, Phys. Rev. Lett. **117**, 193202 (2016).

[17] B. H. Schaap, S. Schouwenaars, and O. J. Luiten, A Raman quantum free-electron laser model, Phys. Plasmas **29**, 113302 (2022).

[18] J. G. H. Franssen, T. L. I. Frankort, E. J. D. Vredenbregt, and O. J. Luiten, Pulse length of ultracold electron bunches

extracted from a laser cooled gas, Struct. Dyn. **4,** 044010 (2017).

[19] B. J. Siwick, A. A. Green, C. T. Hebeisen, and R. J. D. Miller, Characterization of ultrashort electron pulses by electron-laser pulse cross correlation, Opt. Lett. **30,** 1057 (2005).

[20] R. P. Chatelain, V. R. Morrison, C. Godbout, and B. J. Siwick, Ultrafast electron diffraction with radio-frequency compressed electron pulses, Appl. Phys. Lett. **101,** 081901 (2012).

[21] M. Gao, H. Jean-Ruel, R. R. Cooney, J. Stampe, M. de Jong, M. Harb, G. Sciaini, G. Moriena, and R. J. Dwayne Miller, Full characterization of RF compressed femtosecond electron pulses using ponderomotive scattering, Opt. Express **20,** 12048 (2012).

[22] C. T. Hebeisen, R. Ernstorfer, M. Harb, T. Dartigalongue, R. E. Jordan, and R. J. Dwayne Miller, Femtosecond electron pulse characterization using laser ponderomotive scattering, Opt. Lett. **31,** 3517 (2006).

[23] C. T. Hebeisen, G. Sciaini, M. Harb, R. Ernstorfer, T. Dartigalongue, S. G. Kruglik, and R. J. Miller, Grating enhanced ponderomotive scattering for visualization and full characterization of femtosecond electron pulses, Opt. Express **16,** 3334 (2008).

[24] V. R. Morrison, R. P. Chatelain, C. Godbout, and B. J. Siwick, Direct optical measurements of the evolving spatio-temporal charge density in ultrashort electron pulses, Opt. Express **21,** 21 (2013).

[25] S. Tokita, M. Hashida, S. Inoue, T. Nishoji, K. Otani, and S. Sakabe, Single-Shot Femtosecond Electron Diffraction with Laser-Accelerated Electrons: Experimental Demonstration of Electron Pulse Compression, Phys. Rev. Lett. **105,** 215004 (2010).

[26] S. Banerjee, S. Sepke, R. Shah, A. Valenzuela, A. Maksimchuk, and D. Umstadter, Optical Deflection and Temporal Characterization of an Ultrafast Laser-Produced Electron Beam, Phys. Rev. Lett. **95,** 035004 (2005).

[27] W. J. Engelen, Coherent electron bunches from laser-cooled gases, Department of Applied Physics, Technische Universiteit Eindhoven, 2013.

[28] W. J. Engelen, E. J. D. Vredenbregt, and O. J. Luiten, Analytical model of an isolated single-atom electron source, Ultramicroscopy **147,** 61 (2014).

[29] J. P. McGilligan, P. F. Griffin, E. Riis, and A. S. Arnold, Diffraction-grating characterization for cold-atom experiments, J. Opt. Soc. Am. B **33,** 1271 (2016).

[30] C. C. Nshii, M. Vangeleyn, J. P. Cotter, P. F. Griffin, E. A. Hinds, C. N. Ironside, P. See, A. G. Sinclair, E. Riis, and A. S. Arnold, A surface-patterned chip as a strong source of ultracold atoms for quantum technologies, Nat. Nanotechnol. **8,** 321 (2013).

[31] T. C. H. d. Raadt, Ultra-cold electron source, ponderomotive measurement of self-compression, Master's thesis, Coherence and Quantum Technology, Technische Universiteit Eindhoven, 2019.

[32] See Supplemental Material at http://link.aps.org/supplemental/10.1103/PhysRevLett.130.205001 for the temporal pre-alignment procedure, a more detailed discussion of contributions to the bunch length, the simplified photoionization model, the ionization wavelength spectra, an analysis of instrumental broadening and space charge

effects, and a table comparing different ultrafast electron diffraction sources, which includes Refs. [33–45].

[33] J. R. Dwyer, C. T. Hebeisen, R. Ernstorfer, M. Harb, V. B. Deyirmenjian, R. E. Jordan, and R. J. D. Miller, Femtosecond electron diffraction: Making the molecular movie, Phil. Trans. R. Soc. A **364,** 741 (2006).

[34] P. L. E. M. Pasmans, Ultrafast electron diffraction: An investigation of fundamental limits, Department of Applied Physics, Technische Universiteit Eindhoven, 2014.

[35] J. G. H. Franssen, An ultracold and ultrafast electron source, Department of Applied Physics—Quantum and Coherence Technology, Eindhoven University of Technology, 2019.

[36] A. J. McCulloch, B. M. Sparkes, and R. E. Scholten, Cold electron sources using laser-cooled atoms, J. Phys. B **49,** 164004 (2016).

[37] B. J. Siwick, J. R. Dwyer, R. E. Jordan, and R. J. Miller, An atomic-level view of melting using femtosecond electron diffraction, Science **302,** 1382 (2003).

[38] M. Harb, R. Ernstorfer, C. T. Hebeisen, G. Sciaini, W. Peng, T. Dartigalongue, M. A. Eriksson, M. G. Lagally, S. G. Kruglik, and R. J. D. Miller, Electronically Driven Structure Changes of Si Captured by Femtosecond Electron Diffraction, Phys. Rev. Lett. **100,** 155504 (2008).

[39] G. Sciaini, M. Harb, S. G. Kruglik, T. Payer, C. T. Hebeisen, F.-J. M. z. Heringdorf, M. Yamaguchi, M. H.-v. Hoegen, R. Ernstorfer, and R. J. D. Miller, Electronic acceleration of atomic motions and disordering in bismuth, Nature (London) **458,** 56 (2009).

[40] S. Tokita, S. Inoue, S. Masuno, M. Hashida, and S. Sakabe, Single-shot ultrafast electron diffraction with a laser-accelerated sub-MeV electron pulse, Appl. Phys. Lett. **95,** 111911 (2009).

[41] R. Li, W. Huang, Y. Du, L. Yan, Q. Du, J. Shi, J. Hua, H. Chen, T. Du, H. Xu *et al.*, Note: Single-shot continuously time-resolved MeV ultrafast electron diffraction, Rev. Sci. Instrum. **81,** 036110 (2010).

[42] P. Musumeci, J. T. Moody, C. M. Scoby, M. S. Gutierrez, H. A. Bender, and N. S. Wilcox, High quality single shot diffraction patterns using ultrashort megaelectron volt electron beams from a radio frequency photoinjector, Rev. Sci. Instrum. **81,** 013306 (2010).

[43] T. van Oudheusden, P. L. E. M. Pasmans, S. B. van der Geer, M. J. de Loos, M. J. van der Wiel, and O. J. Luiten, Compression of Subrelativistic Space-Charge-Dominated Electron Bunches for Single-Shot Femtosecond Electron Diffraction, Phys. Rev. Lett. **105,** 264801 (2010).

[44] M. W. v. Mourik, W. J. Engelen, E. J. D. Vredenbregt, and O. J. Luiten, Ultrafast electron diffraction using an ultracold source, Struct. Dyn. **1,** 034302 (2014).

[45] R. W. Speirs, C. T. Putkunz, A. J. McCulloch, K. A. Nugent, B. M. Sparkes, and R. E. Scholten, Single-shot electron diffraction using a cold atom electron source, J. Phys. B **48,** 214002 (2015).

[46] Amsterdam Scientific Instruments (ASI), https://www.amscins.com/buy-here/cheetah/.

[47] T. Poikela, J. Plosila, T. Westerlund, M. Campbell, M. D. Gaspari, X. Llopart, V. Gromov, R. Kluit, M. v. Beuzekom, F. Zappon *et al.*, Timepix3: A 65 K channel hybrid pixel readout chip with simultaneous ToA/ToT and sparse readout, J. Instrum. **9,** C05013 (2014).

[48] Pulsar Physics, General Particle Tracer, www.pulsar.nl/gpt.

[49] G. M. Lankhuijzen and L. D. Noordam, Streak-Camera Probing of Rubidium Rydberg Wave Packet Decay in an Electric Field, Phys. Rev. Lett. **76**, 1784 (1996).

[50] O. Fedchenko, S. Chernov, G. Schönhense, R. Hahn, and D. Comparat, Narrow-band pulsed electron source based on near-threshold photoionization of Cs in a magneto-optical trap, Phys. Rev. A **101**, 013424 (2020).

[51] F. Zhou, J. Williams, and C.-Y. Ruan, Femtosecond electron spectroscopy in an electron microscope with high brightness beams, Chem. Phys. Lett. **683**, 488 (2017).